iScience

CellPress
OPEN ACCESS

Article

In situ interfacial architecture of lithium vanadate-based cathode for printable lithium batteries

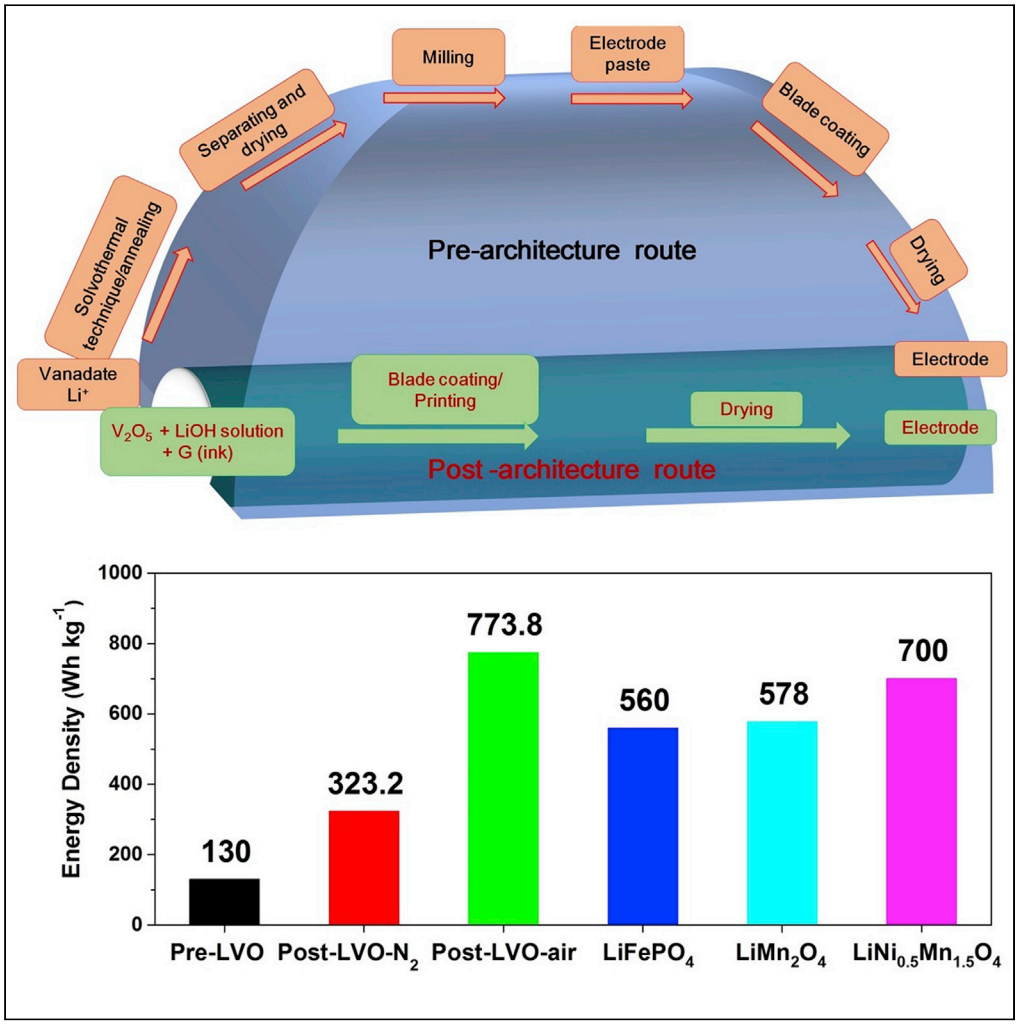

Zhuangzhuang Wang, Wenwei Sun, Dejian Tang, Weilin Liu, Fancheng Meng, Xiangfeng Wei, Jiehua Liu

liujh@hfut.edu.cn

Highlights

Post-architecture route is proposed to *in situ* obtain L_3VO_4-based electrodes in air

The preparation time is shortened to less than 4 hr from 48 to 72 hr

The electrode has a superior reversible capacity of 865.4 mA h g^{-1}

The printable cathode has an energy density of 774 Wh kg^{-1} for low-voltage Li cells

Wang et al., iScience 24, 102666
June 25, 2021
https://doi.org/10.1016/j.isci.2021.102666

iScience

CellPress
OPEN ACCESS

Article

In situ interfacial architecture of lithium vanadate-based cathode for printable lithium batteries

Zhuangzhuang Wang,[1,5] Wenwei Sun,[1,5] Dejian Tang,[1,5] Weilin Liu,[1] Fancheng Meng,[1,2] Xiangfeng Wei,[3] and Jiehua Liu[1,2,4,6,*]

SUMMARY

Most Li_3VO_4 anodes are obtained by pre-architecture methods in which Li_3VO_4 anode materials are prepared with more than six key processes including high-temperature annealing and long preparation time. Herein, we propose an *in situ* post-architecture strategy including Li_3VO_4-precursor solution (ink) preparation and then annealing at 250°C. The integrated Li_3VO_4 based electrode not only possesses good electrical conductivity and porous microstructure but also has superior stability because of Cu anchoring and inclusion by *in situ* catalysis. The integrated electrode demonstrates a high reversible capacity (865 mA h g^{-1} at 0.2 A g^{-1}) and good cyclability (100% capacity retention after 200 cycles at 1 A g^{-1}). More importantly, the post-architecture electrode has a high energy density of 773.8 Wh kg^{-1}, much higher than reported Li_3VO_4-based materials, as well as most cathodes. Therefore, the electrode could be used to the printable cathode of low-voltage high-energy-density lithium batteries.

INTRODUCTION

Metal vanadates have caused wide interest because of their low cost, high specific capacity, and electric-neutrality structures for lithiation/delithiation (Ni et al., 2019; Liu et al., 2019). Compared to commercial graphite and lithium titanate, lithium-rich vanadates have attracted much attention due to low volume swelling and stable cycling, safe working potential, and high energy density (Mo et al., 2017; Liao et al., 2017; Liang et al., 2020). Very recently, disordered rock salt $Li_3V_2O_5$ was synthesized by V_2O_5 lithiation, which exhibits reversibly cycle two Li ions with a specific capacity of 266 mA h g^{-1}(Liu et al., 2020a). Li_3VO_4 possesses the desired Li^+ insertion potential and a high theoretical capacity of 394 and 593 mA h g^{-1} when two and three electrons transfer, respectively (Xu et al., 2019; Liang et al., 2015). Peapod-like Li_3VO_4/N-doped carbon nanowires were synthesized through a morphology-inheritance route, displaying a high reversible capacity of about 400 mA h g^{-1} at 0.1 A g^{-1} (Shen et al., 2017b). Deflated balloon-like Li_3VO_4/C/reduced graphene oxide (LVO/C/rGO) microspheres were prepared by the "double-carbon decoration" strategy for improving their electrical conductivity and enduring 20% volume swelling when deep discharging/charging (Liu et al., 2018). LVO/C/rGO exhibited a high intercalation capacity of 591 mA h g^{-1} under discharging/charging range of 0.02–3.0 V.

However, most of Li_3VO_4 anodes are obtained by pre-architecture methods in which anode materials are prepared at high temperatures in advance, and then the electrodes are constructed (Scheme S1).(Shen et al., 2017a; Chen et al., 2015; Li et al., 2015) Pre-architecture methods are common routes for preparing electrodes of energy storage devices, but there are more than six key processes to obtain the electrodes with a long time of 2–3 days including solvothermal process/annealing, separating, drying, milling, stirring, coating, vacuum drying, and so on. The preparation processes are not only complex but also high energy consumption. The annealing temperatures are often higher than 500°C (Iwama et al., 2016; Huang et al., 2019). On the other hand, Li_3VO_4-based electrodes are often used as an anode in lithium-ion batteries (Zhang et al., 2016b; Qin et al., 2019). Their potential applications have been neglected as cathodes in lithium batteries. Low-voltage lithium batteries will have more and more market demand with the development of small electronic components and devices, but they require a high energy density.

[1]Future Energy Laboratory, School of Materials Science and Engineering, Hefei University of Technology, Hefei 230009, China

[2]Engineering Research Center of High-Performance Copper Alloy Materials and Processing, Ministry of Education, Hefei 230009, China

[3]School of Chemistry and Chemical Engineering, Hefei University of Technology, Hefei 230009, China

[4]Key Laboratory of Advanced Functional Materials and Devices of Anhui Province, Hefei University of Technology, Hefei 230009, China

[5]These authors contributed equally

[6]Lead contact

*Correspondence: liujh@hfut.edu.cn

https://doi.org/10.1016/j.isci.2021.102666

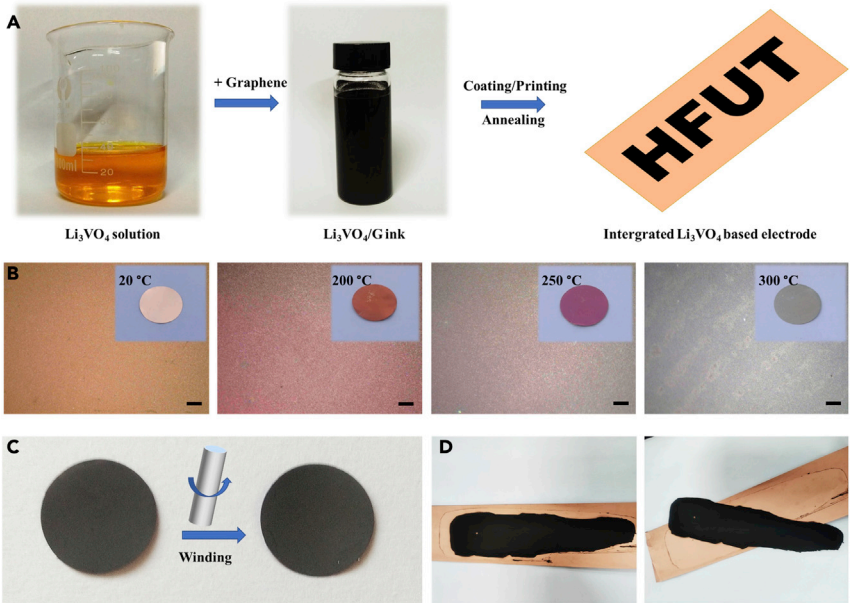

Figure 1. Integrated Li_3VO_4-based electrodes

(A) Schematic illustration of the electrode.

(B) Micrographs and photographs (inset) of Cu foils annealed at 20, 200, 250, 300°C. Scale bar, 200 μm.

(C) The bend test of the post-LVO-air electrode obtained by post-architecture before bending and after bending 1,000 times.

(D) The bend test of the pre-LVO electrode obtained by pre-architecture before and after 1-cycle winding.

Herein, we proposed a post-architecture strategy including Li_3VO_4-precursor-solution (ink) preparation and annealing at 250°C for 1-3 hr (Scheme S1). The integrated Li_3VO_4-based electrode was obtained with good electrical conductivity and porous microstructure, which can endure 1000-time bending because of the *in situ* catalysis of interfacial Cu to Cu(I) and Cu(II) anchoring Li_3VO_4. Moreover, the preparation time is reduced from 48 hr to less than 4 hr. As cathode, the integrated electrode demonstrated high specific capacity (higher than 865 mA h g^{-1} at 200 mA g^{-1}) and good cyclability with 100% capacity retention (547 mA h g^{-1} after 200 cycles at 1,000 mA g^{-1}). More importantly, the integrated Li_3VO_4 based electrode has a higher energy density (773.8 Wh kg^{-1}) than the most reported cathodes (500-700 Wh kg^{-1}) and could be used as a potential cathode in printable high-energy-density lithium batteries.

RESULTS

Post-architecture of integrated Li_3VO_4 based electrodes

Figure 1A is a schematic illustration of an integrated Li_3VO_4-based electrode. First, the Li_3VO_4 precursor solution was obtained by mixing the V_2O_5 and LiOH in an H_2O solution. After a few-layer graphene solution was added, the ink was formed when part of the solvent (H_2O) is evaporated. Then the ink could be coated or printed on Cu foil and then the integrated Li_3VO_4-based electrodes (post-LVO-air and post-LVO-N_2) were obtained after facile annealing at 250°C in the air (Figure S1) and 300°C in N_2, respectively. If no otherwise specified, the above-obtained samples are named post-LVO-air and post-LVO-N_2.

To test the stability of copper foil, bare Cu foils were annealed at different temperatures from 20 to 300°C in the air (Figure 1B). The surface of the copper foil is not oxidized significantly below 150°C because of no color change, while the surface of the copper foil is slightly oxidized when annealed at 200 and 250°C. The copper foil is oxidized significantly when annealing at 300°C. The copper foil is oxidized significantly and its color turns gray on the surface. The result was also supported by their resistance variation (Figure S2). The resistance of Cu foil annealed at 300°C has increased greatly. Therefore, we mainly characterize the post-LVO-air at 250°C. Figure 1C shows the post-LVO-air electrode is highly stable because no active

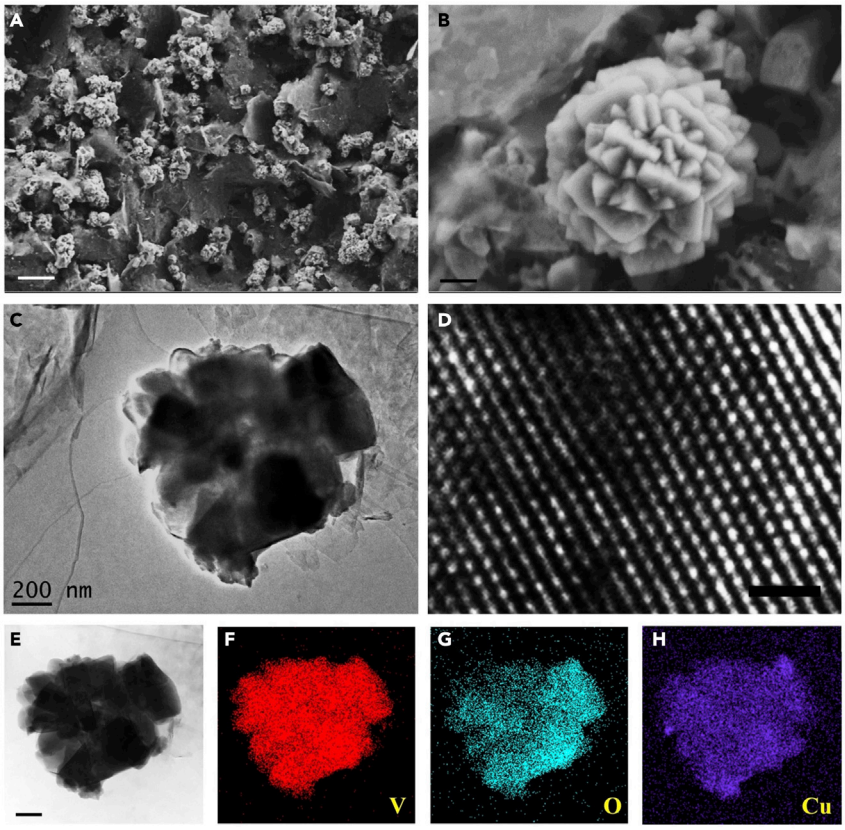

Figure 2. Morphologies and elemental analysis

(A) FESEM image of integrated Li_3VO_4 based electrode. Scale bar, 2 μm.

(B) Enlarged FESEM image of integrated Li_3VO_4-based electrode. Scale bar, 200 nm.

(C) TEM image of integrated Li_3VO_4-based electrode. Scale bar, 200 nm.

(D) HRTEM image of integrated Li_3VO_4-based electrode. Scale bar, 1 nm.

(E) STEM image of integrated Li_3VO_4-based electrode. Scale bar, 200 nm.

(F) V elemental mapping of integrated Li_3VO_4-based electrode.

(G) O elemental mapping of integrated Li_3VO_4-based electrode.

(H) Cu elemental mapping of integrated Li_3VO_4-based electrode.

materials fall off after 1000-time bending with a curvature radius of 3 mm. Video S1 is the bend test of the post-LVO-air electrode related to Figure 1. However, the pre-LVO, which was pure Li_3VO_4 obtained at 300°C in N_2, was peeled off easily from Cu foil when first bending in Figure 1D.

Morphologies and elemental analysis

The morphologies of Li_3VO_4-based electrodes were characterized by field emission scanning electron microscopy (FESEM), transmission electron microscopy (TEM), and scanning transmission electron microscopy (STEM). Figures 2A and 2B show FESEM images of post-LVO-air, which has two-dimensional Li_3VO_4/G nanosheets and flower-like Li_3VO_4 on the surface. Flower-like Li_3VO_4/G could offer high electron conduction, endure the volume swelling when lithium storage, and facilitate the contact of the electrolyte with the electrodes. Figure S3 shows the post-LVO-N_2 has a similar morphology to that of post-LVO-air.

Figure 2C is a TEM image of post-LVO-air which indicates that the porous structure was formed by stacked Li_3VO_4 nanocrystals supporting each other. Figure 2D is the HRTEM image of post-LVO-air that shows the Li_3VO_4 plane is (002) with a lattice space of 0.249 nm. STEM image also supports the non-solid-core flower-like Li_3VO_4 microsphere (Figure 2E). Figures 2F–2H are V, O, and Cu mappings of post-LVO-air. V and O atoms have a uniform dispersion in flower-like Li_3VO_4, suggesting Li_3VO_4 is the main composition on the

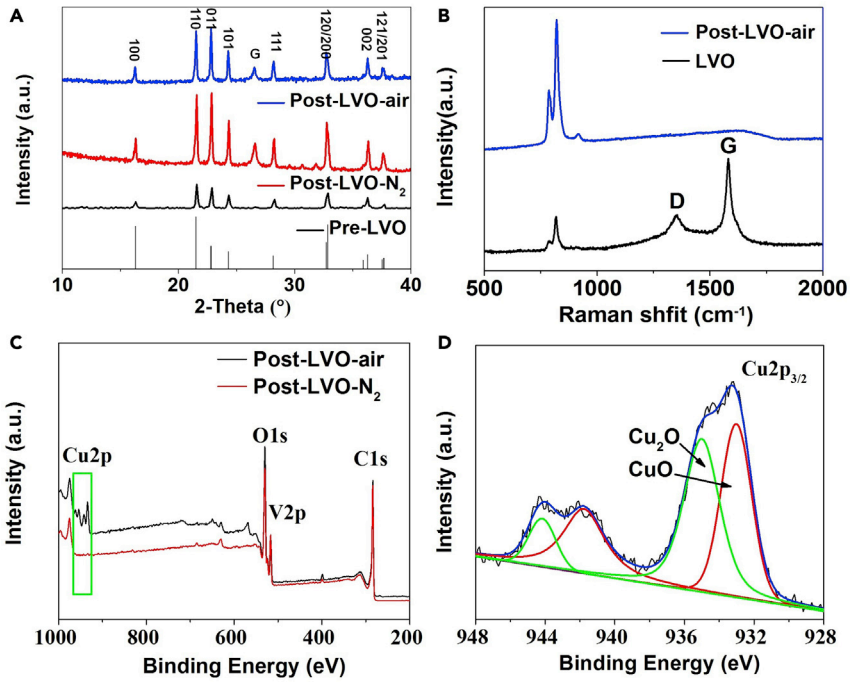

Figure 3. Structures and composition properties of Li_3VO_4-based electrodes

(A) XRD patterns of pre-LVO, post-LVO-N_2, and post-LVO-air.

(B) Raman spectra of pre-LVO and post-LVO-air.

(C) Full XPS spectra of post-LVO-N_2 and post-LVO-air.

(D) Fitted Cu2$p_{3/2}$ XPS spectra of post-LVO-air.

surfaces. Interestingly, Cu atoms have a uniform dispersion, as well as V and O atoms, indicating V_2O_5 or lithium vanadate could catalyze Cu to Cu ions which were incorporated in Li_3VO_4 electrode.

Structures and composition properties of Li_3VO_4 based electrodes

Powder X-ray diffraction (XRD) is used to investigate the crystal structures and components of Li_3VO_4-based electrodes including pre-LVO, post-LVO-N_2, and post-LVO-air. In Figure 3A, pre-LVO has the characteristic peaks of orthorhombic Li_3VO_4 (PDF#38-1,247) (Zhang et al., 2016c). Post-LVO-N_2 has the same peaks as the post-LVO-air. The peaks of post-LVO-N_2 at 26.53° is corresponding to the (002) peak of the graphitized carbon (Wang et al., 2018a). Moreover, the diffraction peaks at 16.45°, 21.67°, and 22.98° are assigned to (100), (110), and (011) planes of Li_3VO_4, which has smaller lattices than that of post-LVO-air at 16.26°, 21.52°, and 22.80°(Zhang et al., 2016a; Wang et al., 2018b). The cell volume of post-LVO-air increases, which was caused by Cu ion doping. There is a shift of (110) peak from 21.56 (post-LVO-N_2 and pre-LVO) to 21.52° for post-LVO-air (Figure S4). Moreover, there is crystal-oriented growth along <011 > direction because of I_{011}/I_{110} ratio of 1.04 for post-LVO-air, larger than that of 0.45 for pre-LVO. However, there are no peaks for CuO or Cu_2O crystals.

Raman spectra were tested to investigate the structural features of pre-LVO and post-LVO-air. In Figure 3B, the peak at 1,352 cm^{-1} is assigned to defects and disorder (D band) of graphene in the post-LVO-air. The strong peak at 1,582 cm^{-1} is related to the vibration of the sp^2 bond as same as graphite (G band). The peak intensity ratio (I_D/I_G) is 0.35 indicating that the few-layer graphene has fewer defects and can be used as the conductive reagent. Raman spectra were tested to analyze the stretching and bending vibration of VO_4^{3-} anions. The band appearing at about 821 cm^{-1} is attributed to symmetric stretching of (VO_4^{3-}), whereas the band at around 786 cm^{-1} is assigned to asymmetric stretching of (VO_4^{3-}) (Yang et al., 2018).

X-ray photoelectron spectroscopy (XPS) was employed to analyze the chemical composition and surface chemical bonding state of post-LVO based electrodes. In Figure 3C, XPS survey spectra show that Cu, O, V, and C elements can be recognized in post-LVO-air, while O, V, and C elements were indexed in

post-LVO-N_2 (Zhou et al., 2017). Post-LVO-air has a Cu content of 2.0 atom%. We think that V_2O_5 could *in situ* catalyze Cu (0) to Cu(II) or Cu(I) on the surface of Cu foil which not only strongly rivet Li_3VO_4 on Cu foil but also doped into the lattices of Li_3VO_4. The high-resolution Cu $2p_{3/2}$ spectrum was fitted into two peaks that correspond to Cu(II) (933.0 eV) and Cu(I) (435.0 eV), which also were supported by the satellite peak at 941.8 and 944.2 eV (Figure 3D).(Pei et al., 2017; Ma et al., 2008) High-resolution V 2p spectrum corresponds to V(V) in VO_4^{3-} at 517.3 eV (Figure S5). In Figure S6, the fitted O 1s peaks at 530 and 532 eV are ascribed to Cu-O/V-O and adsorbed oxygen and C-O, respectively.

Figure S7 shows the results of cyclic voltammetry (CV) tests of post-LVO-N_2 at a scan rate of 0.5 mV s^{-1} for the first five cycles. The initial discharge profile is different from the followed cycles because of the formation of SEI film at 0.65 V (Ren et al., 2020). In the third to fifth cycles, two reduction peaks around 0.9 and 0.5 V are attributed to the corresponding reduction of V^{5+} to V^{3+} and Li^+ insertion into the anode (Liu et al., 2018). The oxidation peak centered at about 1.3 V is attributed to the Li^+ extraction and the oxidation of V^{3+} to V^{5+}(Hu et al., 2016). Figure S8 is the CV curves of pre-LVO with a similar test condition. Because the pre-LVO was dried at 120°C, there are a pair of weak redox peaks at 2.6 and 1.7 V indicating Cu(II) was involved in the electrochemical test.

Electrochemical performance of Li_3VO_4-based electrodes

Figures 4A and 4B shows the typical galvanostatic discharge-charge curves of post-LVO-N_2 at 200 mA g^{-1} within the potential window of 0.01–3 V. The post-LVO-N_2 has discharge capacities of 695.1 and 494 mA h g^{-1} for the first and third cycles, which is perfectly in consistence with the CV measurements. However, the pre-LVO electrode only has capacities of 557 and 254.1 mA h g^{-1}, much less than these of post-LVO-N_2. The post-LVO-N_2 and pre-LVO electrodes are tested at low and high rates to investigate their cycling performance. Figure S9 exhibits excellent cycle performances at a current density of 200 mA g^{-1}. Post-LVO-N_2 delivers a high reversible capacity of 482.4 mA h g^{-1} after 100 cycles, the capacity retention is 100% compared to that in the fifth cycle. Moreover, the Coulombic efficiency approaches 100% after activation in the first five cycles.

After 3 cycles activation at 0.5 A g^{-1}, there is a capacity of 258.4 mA h g^{-1} at a high rate of 2 A g^{-1} in Figure S10. The capacity is still 234.6 mA h g^{-1} with a capacity retention of 91% after 600 cycles. Different rate performances are also provided in Figure 4C. There are the retention capacities of 478.8, 390.2, 317.9, 254.5, 211.9, and 464.2 mA h g^{-1} for post-LVO-N_2, much higher than the capacities of 298.9, 240.0, 178.7, 119.3, 91.4, and 313 mA h g^{-1} for pre-LVO at 0.2, 0.5, 1, 2, 4, and 0.2 A g^{-1}, respectively. We note that Cu ions could be doped into LVO to form $Li_3Cu_xVO_{4+x}$ with an improved capacity when annealing in air.

Therefore, we *in situ* synthesized the post-LVO-air electrodes at 200, 250, and 300°C. Figure S11 shows the CV curve of the post-LVO-air obtained at 200°C. The weak oxidation peak at 2.6 V shows a little Cu inclusion contribute to the capacity of the electrode. The result is supported by its charge-discharge curves, indicating that the capacities are only 631.8 and 424.7 mA h g^{-1} in the first and third cycles (Figure S12). Figure 4D shows the post-LVO-air obtained at 250°C has a strong oxidation peak at 2.6 V, indicating Cu inclusion in the post-LVO-air electrode. In Figure 4E, its capacities are 1,377 and 865.4 mA h g^{-1} in the first and third cycles, much higher than those of post-LVO-air obtained at 250°C. However, the oxidation peak at 2.6 V became weak when annealing at 300°C (Figure S13). The capacities of post-LVO-air obtained at 300°C are 1,457 and 662 mA h g^{-1} in the first and third cycles (Figure S14). That is, the post-LVO-air electrode has the highest reversible capacity when annealing at 250°C. The rate performances of post-LVO-air electrodes are also tested at different temperatures in Figure 4F. The retention capacities of 810.4/759.1, 684.2/651.8, 576.2/533.4, 456.3/418.8, 334.6/295.7, 861.8/807.1 mA h g^{-1} for post-LVO-air obtained at 250/300°C at 0.2, 0.5, 1, 2, 4, and 0.2 A g^{-1}, respectively, much better than those of pre-LVO and post-LVO-N_2.

The resistances of the batteries are elucidated by electrochemical impedance spectra (EIS). The first semicircle in the high-frequency region is related to the impedance of Li ions through the passivation layer on the active material surface (solid-electrolyte interface). In Figure 4G, the post-LVO-air obtained at 250°C has smaller charge-transfer impedances than those of post-LVO-air electrodes obtained at 200 and 300°C according to the first semicircle. After 10 cycles, the impedance becomes smaller than the post-LVO-air based fresh cell (Figure S15). To test their high-rate performance, the post-LVO-air obtained at 250°C was activated at 0.5 A g^{-1} and tested in long-time performance at 1 A g^{-1}. In Figure 4H, the electrode exhibits excellent cycling performance with Coulombic efficiency of 100% at a high rate of 1 A

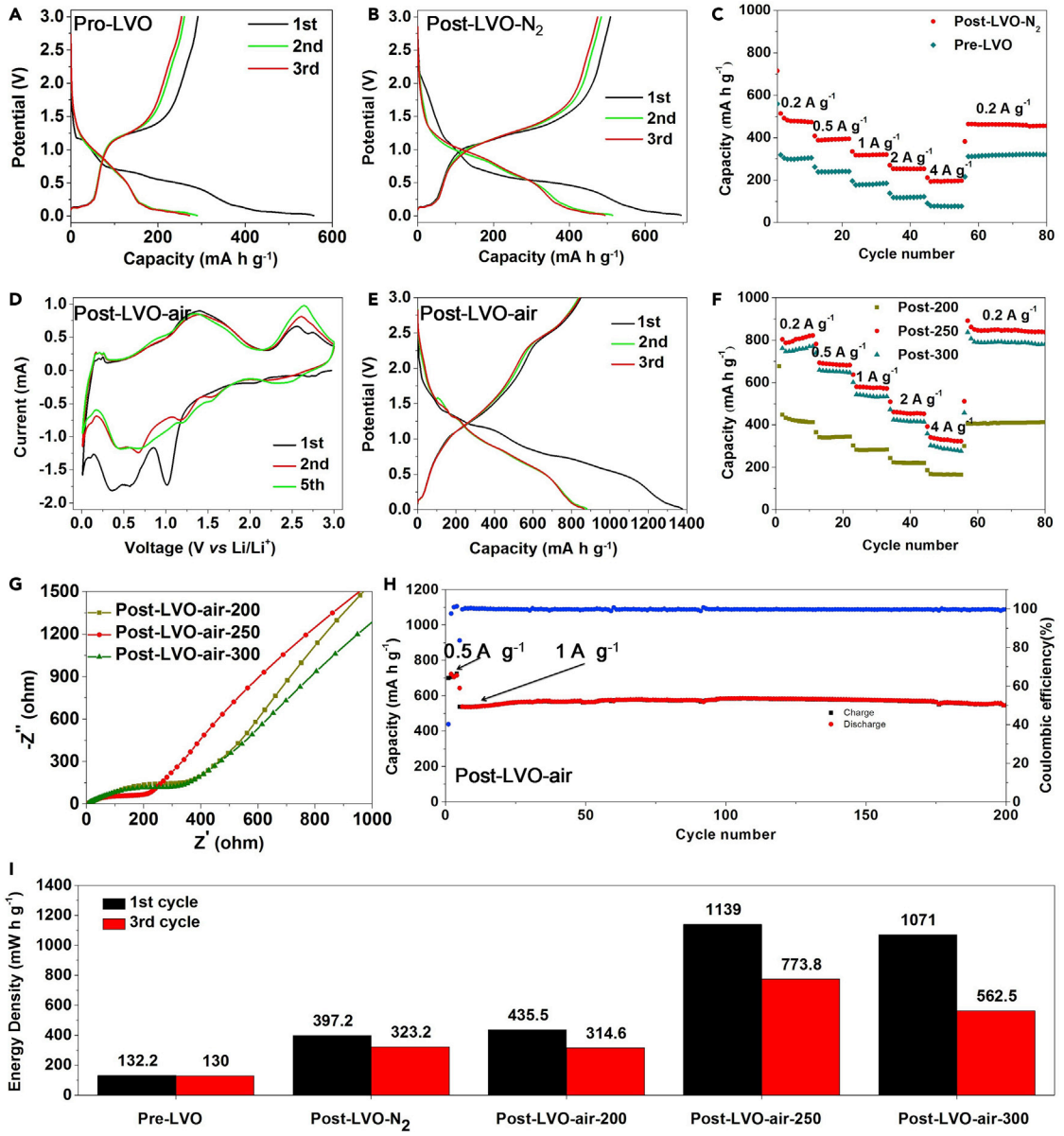

Figure 4. Electrochemical performance of Li_3VO_4-based electrodes

(A) Charge-discharge curves of pre-LVO at 0.2 A g^{-1}.

(B) Charge-discharge curves of post-LVO-N_2 at 0.2 A g^{-1}.

(C) Rate performance of pre-LVO and post-LVO-N_2 at 0.2–4 A g^{-1}.

(D) CV curves of post-LVO-air obtained at 250°C in the air at a scan rate of 0.5 mV s^{-1}.

(E) Charge-discharge curves of post- LVO-air at 0.2 A g^{-1}.

(F) Rate performance of post-LVO-air electrodes at 0.2–4 A g^{-1}.

(G) Nyquist plots of post-LVO-air electrodes.

(H) High-rate performance of post-LVO-air electrodes at 1 A g^{-1}

(I) Energy densities of pre-LVO, post-LVO-N_2, and post-LVO-air electrodes.

g^{-1}. There is still a high capacity of 546.9 mA h g^{-1} after 200 cycles, a little higher than the capacity of 538 after activation in the sixth cycle.

The energy densities were calculated with LVO based electrode as the cathode in lithium batteries. In Figure 4I, the energy densities are provided for pre-LVO, post-LVO-N_2, post-LVO-air obtained at 200, 250, and

300°C. The pre-LVO has energy densities of 132.2 and 130 Wh kg^{-1} at the first and third cycles, which is not suitable for cathode electrodes, less than the theoretical energy density of 271 Wh kg^{-1} for $Li_4Ti_5O_{12}$. The post-LVO-N_2 has a high energy density of 397.2 and 323.2 Wh kg^{-1} at the first and third cycles, but lower than $LiMn_2O_4$ (~560 Wh kg^{-1}) and $LiFePO_4$ (~578 Wh kg^{-1})(Yu et al., 2015). More importantly, the post-LVO-air obtained at 250°C has achieved high energy densities of 1,139 and 773.8 Wh kg^{-1}, higher than post-LVO-air obtained at 200 and 300°C as well as the most of cathodes including high-voltage $LiVPO_4F$ (660 Wh kg^{-1}) and $LiNi_{0.5}Mn_{1.5}O_4$ (700 Wh kg^{-1}) (Xue et al., 2020; Wu et al., 2014). Therefore, the post-LVO-air obtained at 250°C has great potential in low-voltage lithium batteries. Figure S16 shows post-LVO-air based batteries have a specific capacity of 664.4 mA h g^{-1} and an energy density of 732.4 Wh kg^{-1} with a cut-off voltage of 0.5 V.

It should be pointed out that the capacity of pre-LVO-air is much higher than the theoretical capacities (394 and 593 mA h g^{-1}) of Li_3VO_4 for two and three electrons transfer, as well as the most reported works (Table S1).(Liao et al., 2018; Shen et al., 2017a, 2017b; Xu et al., 2019; Ren et al., 2020; Liu et al., 2020b; Huang et al., 2019; Qin et al., 2019) We infer that the Cu ions contribute part of the capacity because Cu(0) was catalyzed to Cu(I) and Cu(II) to form Cu-inclusion LVO (Scheme S2). On the other hand, the surface of Cu foil becomes rougher after Cu surface oxidation which is supported by FESEM image and Cu mapping on the cross-section image of the electrode in Figure S17, and strong Cu-O-V bondings could be formed on the interface of Cu foil, by which Cu-inclusion LVO could be firmly fixed to the copper foil and enhance its cycling performance. The possible reason for improved performance is due to the capacity of copper oxide which may be an amorphous structure in the electrode. Moreover, copper oxide microregions exist on the Cu foil which could anchor the LVO based electrode film and further improve the stability and rate performance.

DISCUSSION

In summary, the integrated Li_3VO_4 based electrode was successfully synthesized by the post-architecture strategy including Li_3VO_4-precursor ink and then annealing at 250°C for 1-3 hr. The preparation time is shortened to ~4 hr, much less than 48-72 hr in pre-architecture methods. The integrated Li_3VO_4 based electrode exhibits good electrical conductivity and superior stability, which could endure 1000-time bending because of Cu anchoring and inclusion in Li_3VO_4 electrode by *in situ* catalysis. Importantly, the integrated electrode demonstrated good cyclability at high rates and high specific reversible capacity (two times as the theoretical capacity of Li_3VO_4). More importantly, the post-LVO-air obtained at 250°C possesses high energy densities of 1,139 and 773.8 Wh kg^{-1} in the first and third cycles, respectively, much higher than pre-LVO, post-LVO-N_2, as well as most of the cathodes. We think the post-LVO-air could be used as the cathode for printable low-voltage high-energy-density lithium batteries due to facile postarchitecture and excellent electrochemical performance.

Limitations of the study

This work focuses on lithium vanadate based cathode by *in situ* interfacial architecture for printable lithium batteries. The integrated electrode demonstrates a high reversible capacity, good cyclability, and a high energy density owing to good electrical conductivity, porous microstructure, and superior stability. Because Cu foil is used as the substrate, we cannot get the precise data of Cu content in the electrode by XPS and Cu mapping characterizations which is a limitation of the work. The electrode capacity is not accurate due to the uncertain Cu ions content. The authors encourage the researchers who are interested in the related work to propose new methods and routes to improve the performance of printable lithium batteries.

STAR★METHODS

Detailed methods are provided in the online version of this paper and include the following:

- KEY RESOURCES TABLE
- RESOURCE AVAILABILITY
  - Lead contact
  - Materials availability
  - Data and code availability
- METHOD DETAILS
  - Preparation of LVO based electrodes

- Characterization
- Electrochemical measurements

SUPPLEMENTAL INFORMATION

Supplemental information can be found online at https://doi.org/10.1016/j.isci.2021.102666.

ACKNOWLEDGMENTS

This work was supported by NSFC-CAS Joint Fund for Research Based on Large-Scale Scientific Facilities, China (grant nos. U1832136), the National Natural Science Foundation of China (grant no. 21303038), Fundamental Research Funds for the Central Universities, China (JZ2020HGQA0149 and PA2020GDGP0054), and National Science Foundation of Anhui and Jiangxi (JZ2018AKZR0058, 20202BAB204007).

AUTHOR CONTRIBUTIONS

J.L., Z.W., W.S., and D.T. conceived the project and designed experiments. All the authors analyzed and interpreted the data. J.L. and Z.W. wrote the manuscript. All the authors discussed the results and commented on the manuscript.

DECLARATION OF INTERESTS

The authors declare no competing interests.

Received: January 12, 2021
Revised: April 8, 2021
Accepted: May 25, 2021
Published: June 25, 2021

REFERENCES

Chen, L., Jiang, X.L., Wang, N.N., Yue, J., Qian, Y.T., and Yang, J. (2015). Surface-amorphous and oxygen-deficient Li_3VO_4-delta as a promising anode material for lithium-ion batteries. Adv. Sci. *2*, 1500090.

Hu, S., Song, Y., Yuan, S., Liu, H., Xu, Q., Wang, Y., Wang, C.-X., and Xia, Y.-Y. (2016). A hierarchical structure of carbon-coated Li_3VO_4 nanoparticles embedded in expanded graphite for high performance lithium ion battery. J. Power Sources *303*, 333–339.

Huang, Y.H., Yang, H.C., Zhang, Y., Zhang, Y.M., Wu, Y.T., Tian, M.K., Chen, P., Trout, R., Ma, Y., Wu, T.H., et al. (2019). A safe and fast-charging lithium-ion battery anode using MXene supported Li_3VO_4. J. Mater. Chem. A *7*, 11250–11256.

Iwama, E., Kawabata, N., Nishio, N., Kisu, K., Miyamoto, J., Naoi, W., Rozier, P., Simon, P., and Naoi, K. (2016). Enhanced electrochemical performance of ultracentrifugation-derived nc-Li_3VO_4/MWCNT composites for hybrid supercapacitors. ACS Nano *10*, 5398–5404.

Li, Q.D., Wei, Q.L., Sheng, J.Z., Yan, M.Y., Zhou, L., Luo, W., Sun, R.M., and Mai, L.Q. (2015). Mesoporous Li_3VO_4/C submicron-ellipsoids supported on reduced graphene oxide as practical anode for high-power lithium-ion batteries. Adv. Sci. *2*, 1500284.

Liang, G., Yang, L., Han, Q., Chen, G., Lin, C., Chen, Y., Luo, L., Liu, X., Li, Y., and Che, R. (2020). Conductive $Li_{3.08}Cr_{0.02}Si_{0.09}V_{0.9}O_4$ anode material: novel "zero-strain" characteristic and superior electrochemical Li^+ storage. Adv. Energy Mater. *10*, 1904267.

Liang, Z.Y., Lin, Z.P., Zhao, Y.M., Dong, Y.Z., Kuang, Q., Lin, X.H., Liu, X.D., and Yan, D.L. (2015). New understanding of Li_3VO_4/C as potential anode for Li-ion batteries: preparation, structure characterization and lithium insertion mechanism. J. Power Sources *274*, 345–354.

Liao, C.Y., Wen, Y.W., Xia, Z.G., Qin, R.H., Liu, X., Yu, Y., Shan, B., Zhai, T.Y., and Li, H.Q. (2018). Si-doping mediated phase control from beta- to gamma-form Li_3VO_4 toward smoothing Li insertion/extraction. Adv. Energy Mater. *8*, 1701621.

Liao, C.Y., Zhang, Q., Zhai, T.Y., Li, H.Q., and Zhou, H.S. (2017). Development and perspective of the insertion anode Li_3VO_4 for lithium-ion batteries. Energy Storage Mater. *7*, 17–31.

Liu, C., Neale, Z., Zheng, J., Jia, X., Huang, J., Yan, M., Tian, M., Wang, M., Yang, J., and Cao, G. (2019). Expanded hydrated vanadate for high-performance aqueous zinc-ion batteries. Energy Environ. Sci. *12*, 2273–2285.

Liu, H.C., Hu, P., Yu, Q., Liu, Z.H., Zhu, T., Luo, W., Zhou, L., and Mai, L.Q. (2018). Boosting the deep discharging/charging lithium storage performances of Li_3VO_4 through double-carbon decoration. ACS Appl. Mater. Interfaces *10*, 23938–23944.

Liu, H.D., Zhu, Z.Y., Yan, Q.Z., Yu, S.C., He, X., Chen, Y., Zhang, R., Ma, L., Liu, T.C., Li, M., et al. (2020a). A disordered rock salt anode for fast-charging lithium-ion batteries. Nature *585*, 63–67.

Liu, X.Q., Li, G.S., Zhang, D., Meng, L.S., Li, B.Y., and Li, L.P. (2020b). F doped Li_3VO_4: an advanced anode material with optimized rate capability and durable lifetime. Electrochimi. Acta *354*, 136655.

Ma, H., Zhang, S., Ji, W., Tao, Z., and Chen, J. (2008). α-CuV_2O_6 nanowires: hydrothermal synthesis and primary lithium battery application. J. Am. Chem. Soc. *130*, 5361–5367.

Mo, J., Zhang, X.M., Liu, J.J., Yu, J.G., Wang, Z.A., Liu, Z.C., Yuan, X.H., Zhou, C.J., Li, R.L., Wu, X.W., and Wu, Y.P. (2017). Progress on Li_3VO_4 as a promising anode material for Li-ion batteries. Chin. J. Chem. *35*, 1789–1796.

Ni, S.B., Liu, J.L., Chao, D.L., and Mai, L.Q. (2019). Vanadate-based materials for Li-ion batteries: the search for anodes for practical applications. Adv. Energy Mater. *9*, 1803324.

Pei, J., Chen, G., Zhang, Q., Bie, C., and Sun, J. (2017). Phase separation derived core/shell structured $Cu_{11}V_6O_{26}/V_2O_5$ microspheres: first synthesis and excellent lithium-ion anode performance with outstanding capacity self-restoration. Small *13*, 1603140.

Qin, P.C., Lv, X.D., Li, C., Zheng, Y.Z., and Tao, X. (2019). Morphology inheritance synthesis of carbon-coated Li_3VO_4 rods as anode for lithium-ion battery. Sci. China Mater. *62*, 1105–1114.

Ren, X., Ai, D., Zhan, C., Lv, R., Kang, F., and Huang, Z.-H. (2020). 3D porous Li_3VO_4@C

composite anodes with ultra-high rate capacity for lithium-ion capacitors. Electrochim. Acta *355*, 136819.

Shen, L.F., Chen, S.Q., Maier, J., and Yu, Y. (2017a). Carbon-coated Li_3VO_4 spheres as constituents of an advanced anode material for high-rate long-life lithium-ion batteries. Adv. Mater. *29*, 1701571.

Shen, L.F., Lv, H.F., Chen, S.Q., Kopold, P., van Aken, P.A., Wu, X.J., Maier, J., and Yu, Y. (2017b). Peapod-like Li_3VO_4/N-doped carbon nanowires with pseudocapacitive properties as advanced materials for high-energy lithium-ion capacitors. Adv. Mater. *29*, 1700142.

Wang, J., Xu, Y., Ding, B., Chang, Z., Zhang, X., Yamauchi, Y., and Wu, K.C.W. (2018a). Confined self-assembly in two-dimensional interlayer space: monolayered mesoporous carbon nanosheets with in-plane orderly arranged mesopores and a highly graphitized framework. Angew. Chem. Int. Ed. *57*, 2894–2898.

Wang, K., Fu, H.Y., Li, Z.Y., Xia, M.Y., Liang, X.Q., Qi, R.J., Cao, G.Z., and Lu, X.M. (2018b). Enhancing the rate performance of a Li_3VO_4 anode through Cu doping. ChemElectroChem *5*, 478–482.

Wu, W.W., Xiang, H.F., Zhong, G.B., Su, W., Tang, W., Zhang, Y., Yu, Y., and Chen, C.H. (2014). Ordered $LiNi_{0.5}Mn_{1.5}O_4$ hollow microspheres as high-rate 5V cathode materials for lithium ion batteries. Electrochim. Acta *119*, 206–213.

Xu, X.N., Niu, F.E., Wang, C.S., Li, Y.J., Zhao, C.L., Yang, J., and Qian, Y.T. (2019). Li_3VO_4 nanoparticles in N-doped carbon with porous structure as an advanced anode material for lithium-ion batteries. Chem. Eng. J. *370*, 606–613.

Xue, X., Xu, Y., and Ma, X. (2020). Elevated energy density and cyclic stability of $LiVPO_4F$ cathode material for high-rate lithium ion batteries. ACS Appl. Energy Mater. *3*, 3553–3561.

Yang, G., Zhang, B.W., Feng, J.Y., Lu, Y., Wang, Z.Q., Aravindan, V., Aravind, M., Liu, J.L., Srinivasan, M., Shen, Z.X., and Huang, Y.Z. (2018). Morphology controlled lithium storage in Li_3VO_4 anodes. J. Mater. Chem. A *6*, 456–463.

Yu, F., Zhang, L., Lai, L., Zhu, M., Guo, Y., Xia, L., Qi, P., Wang, G., and Dai, B. (2015). High electrochemical performance of $LiFePO_4$ cathode material via in-situ microwave exfoliated graphene oxide. Electrochim. Acta *151*, 240–248.

Zhang, C.K., Liu, C.F., Nan, X.H., Song, H.Q., Liu, Y.G., Zhang, C.P., and Cao, G.Z. (2016a). Hollow cuboid Li_3VO_4/C as high-performance anodes for lithium ion batteries. ACS Appl. Mater. Interfaces *8*, 680–688.

Zhang, C.K., Wang, K., Liu, C.F., Nan, X.H., Fu, H.Y., Ma, W.D., Li, Z.Y., and Cao, G.Z. (2016b). Effects of high surface energy on lithium-ion intercalation properties of Ni-doped Li_3VO_4. NPG Asia Mater. *8*, e287.

Zhang, J.C., Ni, S.B., Ma, J.J., Yang, X.L., and Zhang, L.L. (2016c). High capacity and superlong cycle life of Li_3VO_4/N-C hybrids as anode for high performance Li-ion batteries. J. Power Sources *301*, 41–46.

Zhou, J.F., Zhao, B.C., Song, J.Y., Chen, B.Z., Ma, X.H., Dai, J.M., Zhu, X.B., and Sun, Y.P. (2017). Optimization of rate capability and cyclability performance in Li_3VO_4 anode material through Ca doping. Chem. Eur. J. *23*, 16338–16345.

STAR★METHODS

KEY RESOURCES TABLE

REAGENT or RESOURCE	SOURCE	IDENTIFIER
Chemicals, peptides, and recombinant proteins		
Lithium peroxide monohydrate	Sinopharm Chemical Reagent Co. Ltd	CAS1310-66-3
Vanadium pentoxide	Alfa Aesar	CAS 1314-62-1

RESOURCE AVAILABILITY

Lead contact

Further information and requests for resources and reagents should be directed to and will be fulfilled by the Lead Contact, Jiehua Liu (liujh@hfut.edu.cn).

Materials availability

All unique reagents generated in this study have been deposited to the Lead Contact without restriction.

Data and code availability

All of the data supporting this study has been shown in the article and supplemental information. Other related data are available from the corresponding author upon reasonable request.

METHOD DETAILS

Preparation of LVO based electrodes

In a typical post-architecture route, 5 mmol V_2O_5 and 30 mmol $LiOH{\cdot}H_2O$ were added into 20-40 mL distilled water to form a clear yellow solution. The ink was formed after 20 wt% graphene paste was added and evaporated to remove ~70% water. The post-LVO-air electrodes were obtained when the ink was coated or printed on Cu foils and then annealed at 200-300°C. The post-LVO-N_2 electrodes were obtained at the same condition unless annealed at N_2 and 200-400°C.

By doing a contrastive experiment, the pre-LVO electrode was obtained by the pre-architecting route. 5 mmol V_2O_5 and 30 mmol $LiOH{\cdot}H_2O$ were added into 40 mL distilled water to form a clear yellow solution. After removing the water, the white powder (Li_3VO_4) was obtained after annealing at 300°C for 10 hr and milling for 2-3 hr. The Li_3VO_4/G paster was formed after graphene was added and milled for enough time. The pre-LVO electrode was obtained after coating on Cu foil and drying at 100°C for 24 hr. The mass loading is 1.5–2 mg cm^{-2} in the electrode.

Characterization

XRD patterns were performed with a D/MAX2500V diffractometer with Cu-Kα radiation (λ = 1.54056 Å). FESEM images were collected by SU8020 (HITACHI). TEM images and elemental mappings were collected using a JEM 2100F with an HAADF-STEM detector and an Oxford EDS. XPS (ESCLAB250) measurements were carried out by using a monochromated Al Kα X-ray source at the power of 150 W. Raman spectra were collected by employing Lab Raman HR Evolution.

Electrochemical measurements

Electrochemical measurements were carried out in lithium-LVO cells at room temperature. Electrochemical tests were using coin cells (CR2032) with 1 mol/L $LiPF_6$ in EC/DMC (1:1 by volume) as an electrolyte, lithium foil as counter and reference electrodes, and LVO based electrodes as cathodes. All cells were assembled in the Ar-filling glove box. Cyclic voltammograms (CV, 0.01–3 V) curves were measured at a scanning speed of 0.5 mV s^{-1} by electrochemical workstations (DH7000 and CHI760E). The EIS measurements were performed with a 5 mV s^{-1} voltage amplitude over a frequency range of 0.02 Hz–100 kHz. Galvanostatic charge/discharge curves and cycling performance were conducted using a battery tester (Neware CT4008) at different current rates of 0.2 A g^{-1} to 4 A g^{-1}. Energy density was calculated based on the integral area of the discharge curve at different cut-off voltages.